

Theoretical and experimental investigation of near-infrared light propagation in a model of the adult head

Eiji Okada, Michael Firbank, Martin Schweiger, Simon R. Arridge, Mark Cope, and David T. Delpy

Near-infrared light propagation in various models of the adult head is analyzed by both time-of-flight measurements and mathematical prediction. The models consist of three- or four-layered slabs, the latter incorporating a clear cerebrospinal fluid (CSF) layer. The most sophisticated model also incorporates slots that imitate sulci on the brain surface. For each model, the experimentally measured mean optical path length as a function of source-detector spacing agrees well with predictions from either a Monte Carlo model or a finite-element method based on diffusion theory or a hybrid radiosity-diffusion theory. Light propagation in the adult head is shown to be highly affected by the presence of the clear CSF layer, and both the optical path length and the spatial sensitivity profile of the models with a CSF layer are quite different from those without the CSF layer. However, the geometry of the sulci and the boundary between the gray and the white matter have little effect on the detected light distribution.

© 1997 Optical Society of America

Key words: Near-infrared spectroscopy, optical path length, spatial sensitivity profile, oxygenation monitoring.

1. Introduction

Since its first proposal¹ the technique of near-infrared spectroscopy (NIRS) has been increasingly applied for the noninvasive measurement of tissue oxygenation in the brain,²⁻⁶ and several different instruments are now available for clinical monitoring.⁷⁻¹⁰ The development of the quantitative measurement of absorption change by a modified Beer-Lambert law made a significant advance in NIRS studies.¹¹ The quantification of NIRS data requires a knowledge of the optical path length in the tissue, which is considerably farther than the physi-

cal distance between source and detector. Direct time-of-flight measurement with a picosecond pulsed laser and streak camera initially enabled the mean flight time ($\langle t \rangle$), and hence the mean optical path length could be derived experimentally for a rat head,¹¹ an adult head,¹² and a neonatal head^{12,13}; larger studies have recently been completed in which phase-resolved techniques were used.^{14,15} In the NIRS calculations, the head is assumed to be a homogeneous medium, although in reality the source and detection fibers are attached onto the surface of the head, requiring the light to pass through the surface tissue layers such as scalp, skull, and cerebrospinal fluid (CSF) both before and after passing through the brain tissue. The clinically important factors in NIRS monitoring of cerebral oxygenation are the contribution of the absorption change in the brain to the detected signal and the volume of tissue interrogated, and these are obviously affected by the inhomogeneity of the head and the measurement geometry. Because these factors cannot be obtained experimentally, it is vital to be able to predict accurately the light propagation in an inhomogeneous structure, such as the head, by mathematical methods.

Several different mathematical techniques have

When this work was performed, E. Okada, M. Firbank, M. Schweiger, M. Cope, and D. T. Delpy were with the Department of Medical Physics and Bioengineering, University College London, First Floor, Shropshire House, 11-20 Capper Street, London WC1E 6JA, UK. S. R. Arridge was with the Department of Computer Science, University College London, Gower Street, London WC1 6BT, UK. E. Okada is now with the Department of Electronics and Electrical Engineering, Keio University, 3-14-1 Hiyoshi, Kohoku-ku, Yokohama 223, Japan.

Received 8 March 1996; revised manuscript received 12 June 1996.

0003-6935/97/00021-11\$10.00/0

© 1997 Optical Society of America

been used to describe light propagation in scattering tissue, and some preliminary modeling of simple layered structures have shown that the light penetration into deeper regions (e.g., the brain) is strongly affected by the optical properties of the surface layer.^{16–24} The presence of a relatively clear layer (e.g., CSF) that has both low scattering and absorption coefficients has been shown especially to alter the light propagation in the head.^{21,24} However, in almost all these studies, the boundary of each layer has had a simple geometry such as a flat or curved surface that is significantly different from real head structures. More sophisticated models are needed for a rigorous analysis of light propagation in the adult head. For example, the brain surface is actually deeply folded with many CSF-filled sulci, and it is likely that light propagation in the brain is affected by the sulcus structure.

In this study, in a variety of models of the adult head, the effect of both the presence of the surface tissues (including a clear CSF layer) around the brain and the brain anatomy itself have been investigated by the use of solid slab phantoms that consist of layers with different optical properties. The simplest adult head model is a three-layered slab without a clear layer, whereas the most sophisticated model has four layers, including a clear layer together with slots that imitate the sulci. Time point-spread functions for several different detection positions on the outer surface are measured with a picosecond laser and a streak camera, and the effect of the layered structures is evaluated in terms of the mean optical path length. The experimental data are compared with the results of both Monte Carlo (MC) and finite-element calculations, which are also used to predict the mean optical path length in each layer. Because the path of individual photons can be traced in the MC calculation, the spatial sensitivity profile in each model has also been predicted, and the effects of the surface layers on the volume of tissue interrogated in the adult brain by NIRS instruments are discussed.

2. Optical Path in Near-Infrared Spectroscopy

The NIRS technique relies on the application of a modified Beer–Lambert law¹¹ to convert measured variations in attenuation (ΔOD , where OD is the optical density) into quantitative changes in the absorption coefficient ($\Delta\mu_a$) in the tissue. In the modified Beer–Lambert law, the mean optical path length $\langle L \rangle$ replaces the physical distance between the source and the detector:

$$\Delta OD \approx \Delta\mu_a \langle L \rangle = \Delta\mu_a c \langle t \rangle. \quad (1)$$

The mean optical path length is significantly greater than the distance between the source and the detector because of the large amount of scattering in the tissue. Thus *a priori* knowledge of the mean optical path length is needed to quantify the change in absorption by the use of the modified Beer–Lambert law. The mean optical path length can be derived from the mean time of flight $\langle t \rangle$ and the speed of light

c in the tissue. The mean time of flight can be obtained from the temporal point-spread function (TPSF), which is the temporal intensity distribution of a picosecond pulsed light that is broadened because of the different scattering paths in the medium.

Although biological tissue has an inhomogeneous structure, the tissue is assumed to be homogeneous in the modified Beer–Lambert law. If it can be assumed that the inhomogeneous tissue consists of several homogeneous media, a partial mean optical path length can be defined.¹⁹ The partial mean optical path length $\langle L_i \rangle$ is the mean optical path length that the detected light travels within a particular medium i , and the variation in attenuation of the detected light across the tissue can be approximated by the sum of the product of the partial mean optical path lengths and the corresponding absorption coefficient changes in each layer ($\Delta\mu_{ai}$):

$$\Delta OD \approx \sum \Delta\mu_{ai} \langle L_i \rangle. \quad (2)$$

The mean optical path length $\langle L \rangle$, which is the sum of the partial mean optical path length $\sum \langle L_i \rangle$, can be calculated from the experimental TPSF measured with a picosecond pulsed laser system. However, the TPSF contains no direct information about the time that the light has spent in each medium, and hence the partial mean optical path length cannot be obtained experimentally.

If the change in the absorption coefficient in each medium is the same, then the partial mean optical path length indicates the contribution that each medium makes to the change in the output signal. It should, however, be noted that, in general, the changes in absorption in each medium are not the same because of differences in hemoglobin content. For instance, the normal CSF layer contains no hemoglobin, and hence it does not contribute to the change in the output signal. Although the partial mean optical path length indicates the signal contribution of each medium, it does not show the spatial distribution of the volume contributing to the output signal. The volume of tissue interrogated with NIRS instruments can, however, be calculated as the spatial sensitivity profile,²² which is deduced from the accumulated optical path histories of the photons reaching the detector.^{25,26}

3. Methods

A. Adult Head Models

The adult head models used in this study are inhomogeneous slabs that consist of three or four different homogeneous media. The geometries of the models and the optical properties for each layer of the model are shown in Fig. 1 and Table 1, respectively. The simplest three-layered model [Fig. 1(a)] consists of a 12-mm-thick surface layer that imitates the scalp and skull, a 4-mm-thick gray-matter layer, and a white-matter layer. The optical properties for these layers have been chosen from the reported data on the optical properties of tissue.^{27–29} The first four-

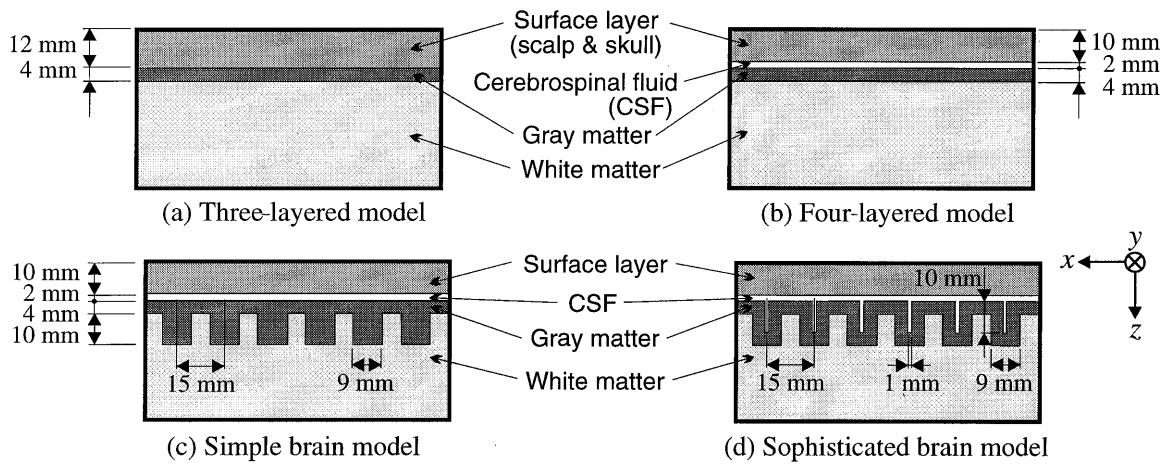


Fig. 1. Schematic designs of the adult head models.

layered model [Fig. 1(b)] has a 2-mm-thick clear layer that imitates the CSF between the 10-mm-thick surface layer and the gray-matter layer. The simplest model of the brain structure [Fig. 1(c)] has an uneven boundary between the gray matter and the white matter. The gray-matter layer has thick areas, 14 mm in thickness and 9 mm in width, placed every 15 mm. In the most sophisticated brain model [Fig. 1(d)], slots 10 mm deep and 1 mm wide that imitate the sulci filled with the clear CSF are added to the simple brain model. The thickness of each layer and the geometry of the sulci and gray matter were chosen from a magnetic resonance image of an adult head.

B. Experimental Setup

The actual design of the adult head phantoms is shown in Fig. 2. The phantom was made of epoxy resin containing TiO_2 to alter its scattering coefficient and IR absorbing dyes to alter its absorption coefficient.³⁰ The phantom for each model consisted of two parts. The surface layer of 10 mm and 12 mm in thickness (which imitated the scalp and skull) formed the front and the rear walls, respectively, of a box filled with glycerol, which imitated the CSF. The second part, a block, 13 cm wide \times 6 cm high \times 8 cm thick, which consisted of the gray-matter and the white-matter layers, could be positioned inside the box at a suitable distance away from the inner face of the front or rear wall. Three different inner blocks were made with gray- and white-matter geometries, as shown in Fig. 1. The three-layered model [Fig.

1(a)] was realized when the inner slab was positioned directly against the inner face of the 12-mm surface layer. The inner slab was located 2 mm away from the inner face of the 10-mm surface layer for all the other models. A picosecond pulsed laser and streak camera were used to measure the TPSF of the phantoms.¹¹ The laser system consisted of an Ar-ion laser pumping a Ti:sapphire laser and streak camera. Laser pulses of approximately 2-ps half-maximum width at the 800-nm wavelength were emitted at 82 MHz. Most of the laser light was delivered to the surface of the phantom while a part of the laser beam was sampled and directly relayed to the streak camera as a time-reference pulse. In the case of the simplest brain model [Fig. 1(c)], the irradiated spot was just over the center of the thick gray matter, and in the sophisticated brain model [Fig. 1(d)], it was in the same position, which now coincided with the center of a slot. The light emerging from the phantom was collected in a fiber bundle and was conveyed to the streak camera. The spacing between the irradiated spot and the fiber bundle was altered horizontally for all the models and also vertically in the case of the models of Figs. 1(c) and 1(d) (i.e., along the thick area of the gray matter or the slot). The TPSF's at each source-detector spacing were measured and stored on a computer. The mean time of flight was calculated from the TPSF, following soft-

Table 1. Optical Properties of the Adult Head Models

Tissue Type	Transport Scattering Coefficient μ_s' (mm^{-1})	Absorption Coefficient μ_a (mm^{-1})
Scalp and skull	2.0	0.04
CSF	0.01	0.001
Gray matter	2.5	0.025
White matter	6.0	0.005

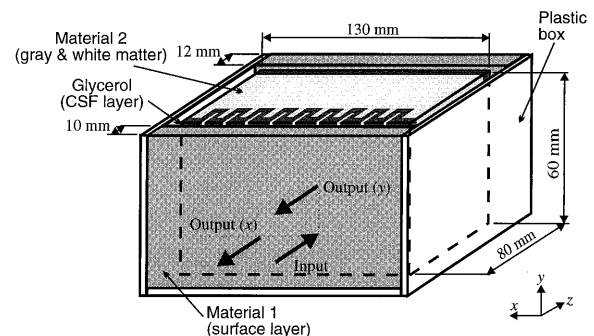


Fig. 2. Construction details for the adult head phantoms.

ware corrections for nonlinearity, shading sensitivity, etc., of the streak camera.

C. Monte Carlo Simulation

The MC algorithm used in this study has already been described¹⁹ and is based on the variance-reduction technique.^{31–33} Isotropic scattering was assumed, and if a photon crossed the boundary between different media, the distance to the next scattering event was corrected by the use of the transport scattering coefficient in the subsequent medium μ_{sj}' :

$$l_j = (l_i - \Delta l)\mu_{si}' / \mu_{sj}', \quad (3)$$

where l_j is the path length to the next scattering from the boundary of the media and Δl is the path length to the boundary of the media from the previous scattering point. In order to avoid dividing by zero in this correction process, a transport scattering coefficient of 0.01 was used for the clear CSF layer. Reflection and refraction of light caused by refractive-index mismatching between the air and the tissue were taken into account.

When the photon was scattered out of the head model, the survival weight of the photon was calculated from the absorption coefficients μ_{ai} and the accumulated partial optical path length in each medium l_i . The survival weight and partial path length of the photon were recorded for each detection position up to a distance of 65 mm from the source. For cases in which the photon reached detection positions of 15, 30, or 40 mm, the history of the photon path weighted by the survival weight was accumulated to obtain the spatial sensitivity profiles.²² The photon paths were projected onto an x - z plane to record the two-dimensional spatial sensitivity profiles. After 10,000,000 input photons were traced, the mean optical path length, partial mean optical path length, the intensity of the detected light normalized by source intensity, and the spatial sensitivity profiles were calculated.

D. Finite-Element Method

The time-independent diffusion equation,³⁴ which is a well-known approximation of the radiative transfer equation,³⁵ has been used to describe light propagation in tissue:

$$-\nabla \cdot \kappa(\mathbf{r})\nabla\Phi(\mathbf{r}) + \mu_a(\mathbf{r})\Phi(\mathbf{r}) = q_0(\mathbf{r}), \quad (4)$$

where $\kappa(\mathbf{r})$ is the diffusion coefficient, $\kappa(\mathbf{r}) = \{3[\mu_a(\mathbf{r}) + \mu_s'(\mathbf{r})]\}^{-1}$, $\Phi(\mathbf{r})$ is the photon density, and $q_0(\mathbf{r})$ is the isotropic source distribution. In this study, a finite-element method^{36,37} (FEM) was used to solve the diffusion equation, and the outgoing fluence (exitance) $\Gamma(\mathbf{r})$ was calculated by

$$\Gamma(\mathbf{r}) = -\kappa(\mathbf{r})\hat{\mathbf{e}} \cdot \nabla\Phi(\mathbf{r}), \quad (5)$$

where $\hat{\mathbf{e}}$ is the vector normal to the detection area.

In order to obtain the partial mean optical path length from the exitance, it is assumed that the optical path length in each layer does not vary with a small absorption change. The difference in exitance

$\Delta\Gamma$ caused by a 1% absorption change in a particular layer i was predicted, and the partial mean optical pathlength $\langle L_i \rangle$ in layer i was calculated by

$$\langle L_i \rangle = \Delta\Gamma / \Delta\mu_{ai}. \quad (6)$$

Although the FEM can be applied to three-dimensional models, in this study a two-dimensional rectangular model was used to keep the memory size required for matrix manipulation within a reasonable limit. For the three-layered model, the rectangular domain was divided into approximately 21,000 triangular subspaces and Robin boundary conditions were used.³⁷ An isotropic point source located at a distance $1/\mu_s'$ below the surface layer at the irradiated position was used to approximate a collimated incident laser beam.³⁷

Because the diffusion equation no longer holds in a medium that has a low scattering coefficient, the FEM could not be directly applied to the models of Figs. 1(b)–1(d) with a clear CSF layer, so a hybrid radiosity–diffusion theory model²⁴ was used instead. The concept of the hybrid radiosity–diffusion model is to predict light propagation in the scattering regions by the diffusion theory and in the clear CSF layer by a radiosity method and to combine the two results in an iterative scheme until a minimum change in exitance is achieved. It is assumed that the light in the scattering tissue, such as scalp, skull, and brain, obeys the diffusion equation (4), and the light propagating without diffusion in the CSF complies with the radiosity equation.²⁴ The FEM was applied to the two rectangular domains, one being the surface layer and the other the gray- and the white-matter layers. The surface and the inner domains were divided into approximately 7000 and 13,000 triangles, respectively. The photon density at the inner boundary of the surface domain arising from the incident beam on its outer surface was first calculated by the FEM, and from this resulting photon density the outgoing radiance $I(p, \mathbf{s})$ at any point p traveling in direction \mathbf{s} on the surface was obtained. With this outgoing radiance, the radiosity theory was used to calculate the resulting irradiance $\Gamma_R(q)$ on an area dA at position q on the outer surface of the inner domain across the clear CSF layer:

$$\Gamma_R(q) = \iint_A \frac{I(p, \mathbf{s})\cos(\theta_1)\cos(\theta_2)}{|\mathbf{r}|^2} \exp(-|\mathbf{r}|\mu_a) dA, \quad (7)$$

where θ_1, θ_2 are the angles between \mathbf{s} and normal components of the surface of the two layers, μ_a is the absorption coefficient of the CSF layer, \mathbf{s} points from p to q . The photon density in the inner domain caused by the irradiance on its surface was then calculated by the FEM, and the resulting outgoing radiance from the inner domain was similarly obtained. The resulting radiance was then again used as an input to the radiosity equation, which calculated the fluence back onto the inner face of the surface domain, and the photon density in the surface layer was recalculated. This process was iterated until the

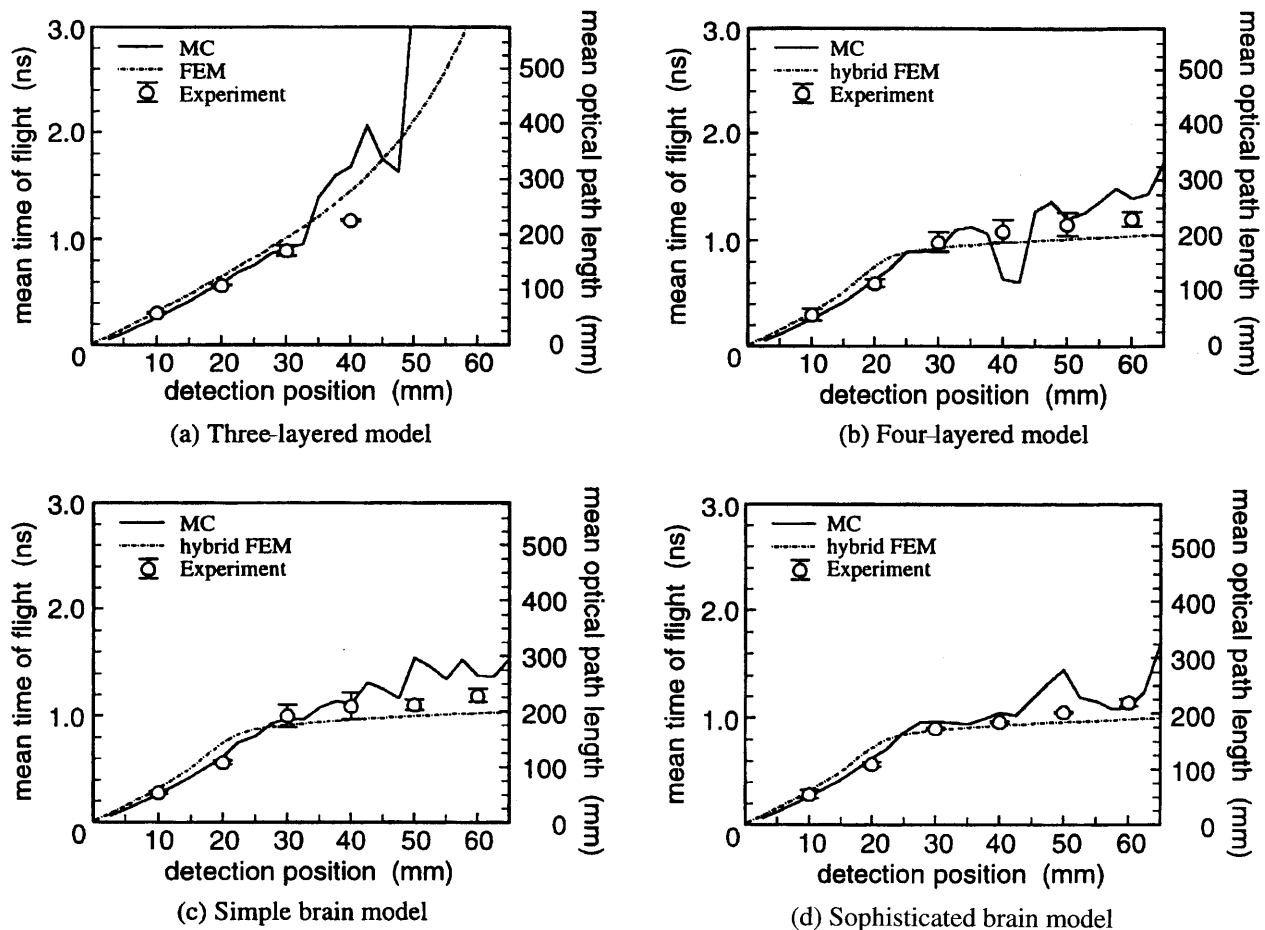


Fig. 3. Mean time of flight and corresponding mean optical path length as functions of the detection position predicted by the MCM and the FEM compared with experimental results (± 1 SD).

change in the total exitance became negligible ($<1\%$ change).

The simple and the sophisticated brain models [Figs. 1(c) and 1(d), respectively] have different cross sections in the $x-z$ and the $y-z$ planes, but the cross section in the $x-z$ plane was used for the two-dimensional approximation for both these models. The partial mean optical path lengths in the models with the clear CSF layers were calculated in the same way as for the three-layered model.

4. Results

Experimental results for the mean time of flight are compared with the predictions of the MC method (MCM) and the FEM in Fig. 3. The corresponding mean optical path length calculated from the mean time and the speed of light in the epoxy resin is also shown in each figure. On a SunSparc 20 workstation, the calculation for each model took ~ 200 -h CPU time for the MCM, 3-min CPU time for the FEM based on the diffusion theory, and 15-min CPU time for the FEM based on the hybrid radiosity-diffusion theory. The experimental results and predictions (MCM and FEM) for the mean time of flight as a function of spacing are in good agreement for all models. However, statistical noise in the MC results is

notable at detection positions of greater than 30 mm. The mean time for all the models at detection positions up to 20 mm are almost the same. For the models of Figs. 1(b)–1(d), which have the clear CSF layer, once the detection position is greater than 20 mm the mean time increases only slowly with spacing between source and detector whereas for the three-layered model [Fig. 1(a)] without the clear layer, it continues to increase rapidly. The differences in mean time between all the models with a clear CSF layer are not significant over the whole range of detection positions. In both the simple brain model [Fig. 1(c)] and the sophisticated brain model [Fig. 1(d)], the direction of the detection position (horizontal or vertical) produced no statistically significant differences in mean time, so data in regard to the vertical detection positions are not shown.

The partial mean optical path length in each layer in the models is shown in Fig. 4. The partial optical path length cannot be obtained from the experimental TPSF, so only the results predicted by the MCM and the FEM are compared. The predictions of both methods show the same tendency. In the three-layered model the partial mean optical path length of both the gray- and the white-matter layers is small at detection positions up to 30 mm. This means that

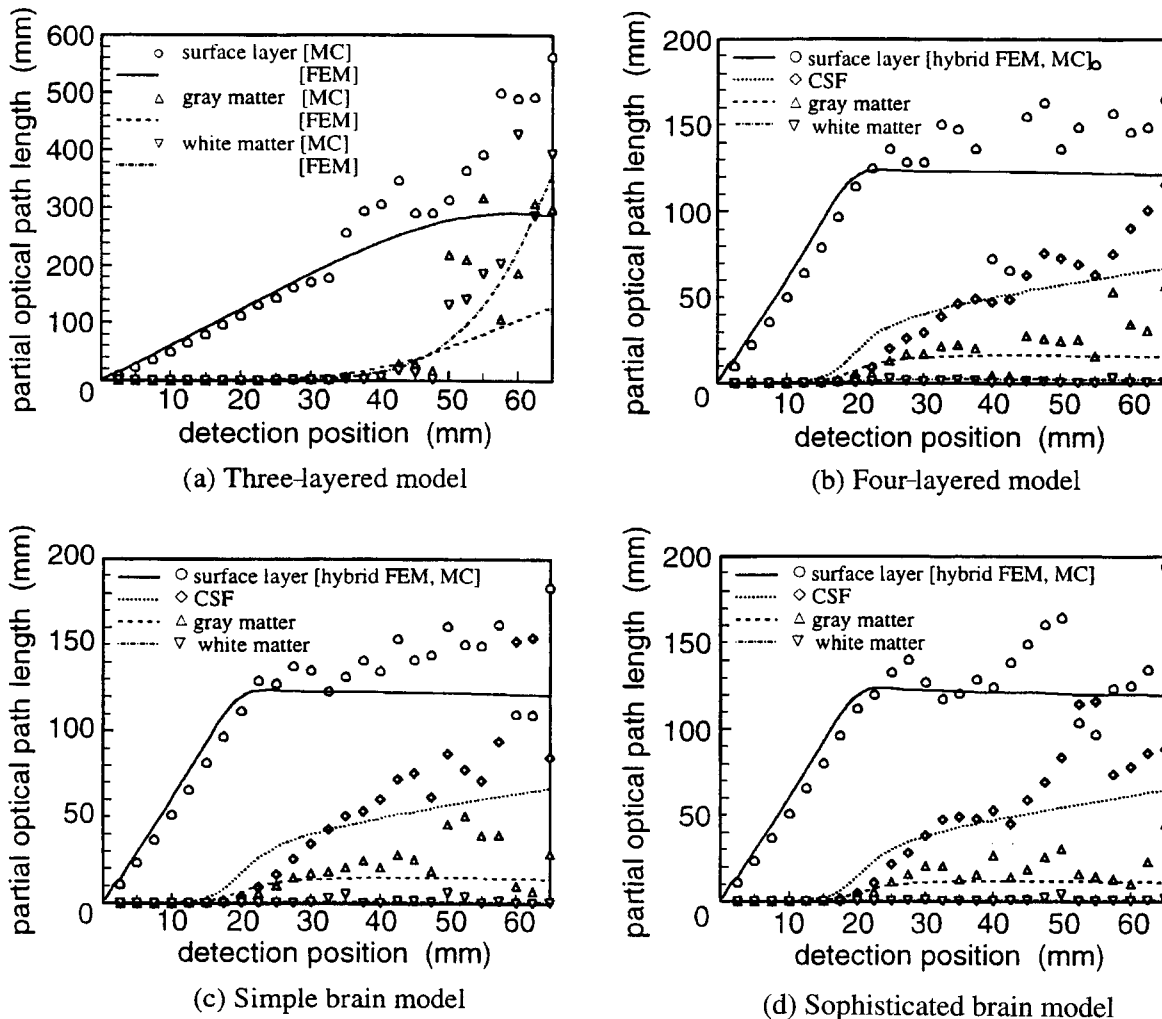


Fig. 4. Partial mean optical path length as a function of detection position predicted by the MCM (symbols) and the FEM (curves).

the light is largely confined to the surface layer. Once the detection position is greater than 30 mm, the partial mean optical path lengths of both the gray- and the white-matter layers (and beyond 50 mm especially the white-matter layer) steeply increase. From the FEM results, the partial mean optical path length of the white-matter layer exceeds that of the surface layer at detection positions of greater than 60 mm. In the models of Figs. 1(b)–1(d) with the clear CSF layer, the relationships between detection position and partial mean optical path lengths are similar, but are completely different from those in the three-layered model of Fig. 1(a). The partial mean optical path lengths of the deeper layers are small at detection positions up to 15 mm. Once the detection position exceeds 15 mm, the partial mean optical path lengths of both the CSF and the gray-matter layer start to increase. The partial mean optical path lengths of both the surface and the gray-matter layers remain almost constant at detection positions of greater than 30 mm, whereas that of CSF layer continues to gradually increase. The partial mean optical path length of the white-matter

layer is still small, even when the detection position exceeds 60 mm.

The intensity of detected light predicted by both the MCM and the FEM is shown in Fig. 5. The results are normalized by the source intensity, and in the case of the simple and the sophisticated brain models [Figs. 1(c) and 1(d), respectively] only the results of horizontal detection are shown. The MCM and FEM predictions agree well for all the models. Up to 20 mm, the intensity for all the models is the same as a function of the detection position. Beyond 20 mm, the rate of decline in the intensity with the detection position for all the models with a clear CSF layer diminishes whereas that for the three-layered model continues at approximately the same rate.

The MC-calculated spatial sensitivity profiles for the three- and the four-layered models [Figs. 1(a) and 1(b), respectively] at a detection position of 15 mm are shown in Figs. 6(a) and 6(b), respectively. The contours are drawn for every 12.5% fall from the maximum sensitivity point, and the extreme contour indicates a relative sensitivity of 0.3%. In both Figs. 6(a) and 6(b) the spatial sensitivity profiles are con-

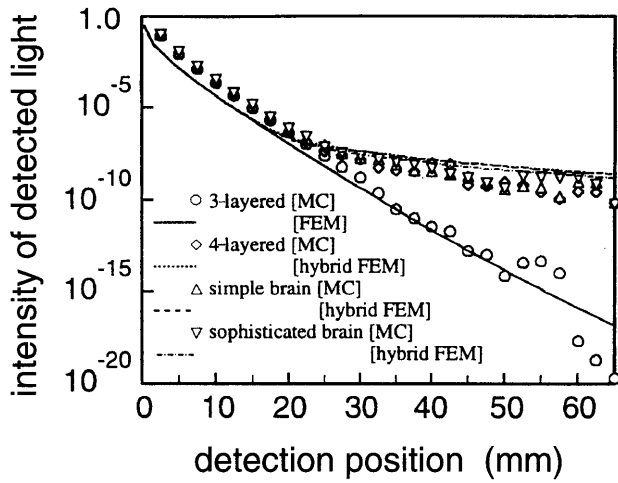
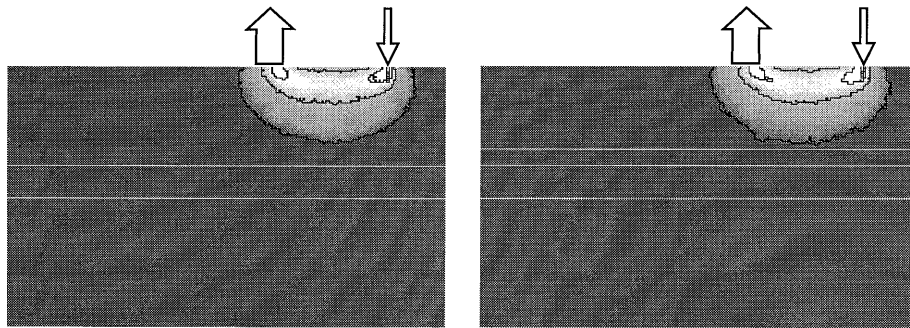


Fig. 5. Normalized intensity of detected light for each model as a function of the detection position predicted by the MCM and the FEM.

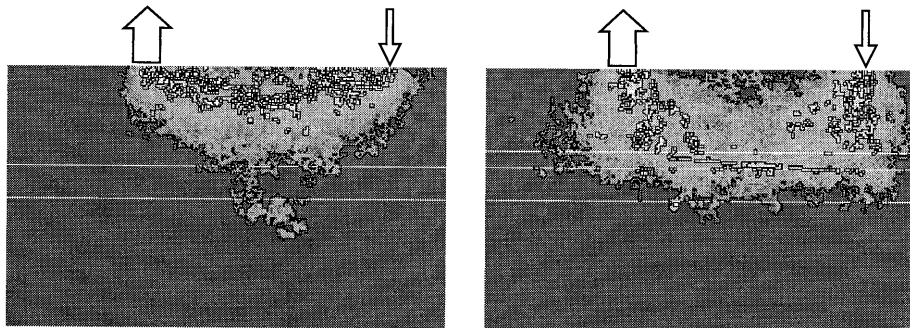
finer to the surface layer, so the results for Fig. 6(b) will also apply to the simple and the sophisticated brain models of Figs. 1(c) and 1(d), respectively, whose differences in the geometry occur only under the CSF layer. Figures 7(a)–7(d) show the spatial sensitivity profiles for all the models at a detection position of 30 mm. In the case of the simple and the sophisticated brain models, the results of horizontal detection are also shown. At this detection position the number of detected photons is not sufficient to provide good statistics; however, the general tendency for the localization of the sensitive area can be recognized. In the three-layered model of Fig. 7(a) the spatial sensitivity profile is still largely confined to the surface layer, and little light penetrates into the gray matter. The spatial sensitivity profile of the four-layered model of Fig. 7(b) spreads farther toward the clear CSF and the gray-matter layers;



(a) Three-layered model

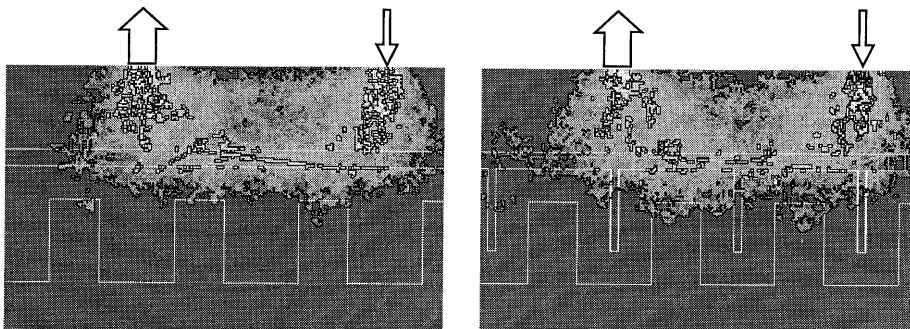
(b) Four-layered model

Fig. 6. Spatial sensitivity profiles with a detection fiber 15 mm distant from the light source along the horizontal (x) axis.



(a) Three-layered model

(b) Four-layered model



(c) Simple brain model

(d) Sophisticated brain model

Fig. 7. Spatial sensitivity profiles with a detection fiber 30 mm distant from the light source along the horizontal (x) axis.

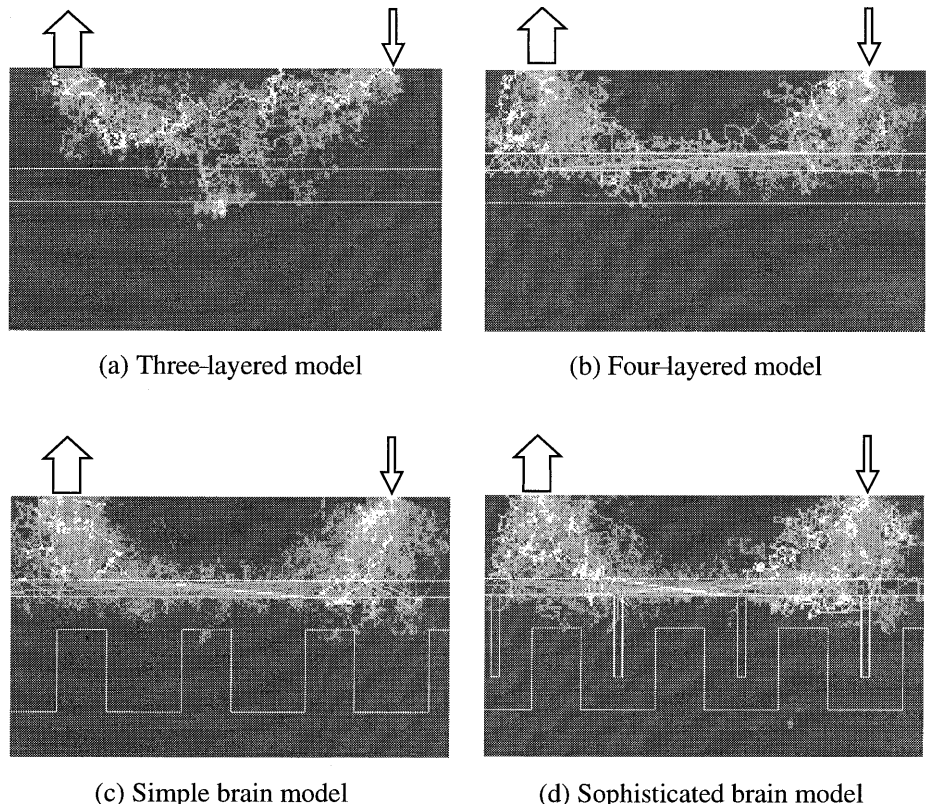


Fig. 8. Spatial sensitivity profiles with a detection fiber 40 mm distant from the light source along the horizontal (x) axis.

however, very little light reaches the white-matter layer. Although light reaches the gray-matter layer, there are no significant differences between the spatial sensitivity profiles of all three models with a clear CSF layer [Figs. 7(b)–7(d)]. The spatial sensitivity profiles at a detection position of 40 mm are shown in Figs. 8(a) and 8(d). Contours have not been drawn on these profiles because of poor statistics. In the three-layered model of Fig. 8(a) the spatial sensitivity profile is still confined mainly to the surface layer. In the other models [Figs. 8(b)–8(d)] the spatial sensitivity profile has shifted toward the deeper layers, and an apparent light path can be seen around the clear CSF layer. However, the detected light still does not tend to penetrate into the white-matter layer. A slight difference in the spatial sensitivity profiles can be observed between the four-layered model of Fig. 8(b), the simple brain model of Fig. 8(c), and the most sophisticated brain model of Fig. 8(d). Finally, Fig. 9 shows the vertical spatial sensitivity profiles of all the models at a detection position of 30 mm. The spatial sensitivity profiles for all the models with a clear CSF layer spread around the CSF layer. The profiles of the four-layered model of Fig. 9(b) and the simple brain model of Fig. 9(c) are almost identical. In the most sophisticated brain model of Fig. 9(d), the source and the detector were positioned above a sulcus, and it can be seen that light penetrates more deeply in the area along the sulcus. However, the spatial sensitivity profile around the sulcus is still confined to the gray-matter layer with little penetration into the white matter.

5. Discussion

In the adult head, experiment has shown that the mean optical path length divided by the spacing between source and detector, the differential path-length factor, is approximately constant for detection positions greater than 25 mm¹² at a value of ~6, but increases at closer detection positions. Because the mean optical path lengths for all the phantoms with a clear CSF layer also show this tendency, the results from these models are thought to reasonably mimic the actual light propagation in the adult head.

In the MCM, the full three-dimensional geometry is faithfully replicated, and therefore the errors in prediction are caused mainly by inadequate photon statistics. The MC results show that although the clear CSF layer increases the intensity of the detected light and hence improves the statistics, significant error is still notable once the detection position is beyond 30 mm. On the other hand, both the normal and the hybrid FEM predictions show reasonable agreement with the experimental results in spite of being only two-dimensional approximations. This indicates that these techniques can probably be used with some confidence to calculate mean optical path lengths in complex heterogeneous media. This is important because, in the practical use of NIRS on the human adult, the fiber spacing is often from 30 to 60 mm, and the statistical error of MC predictions for reasonable computation times is large, beyond a detection position of 30 mm.

The mean optical path lengths for the models with

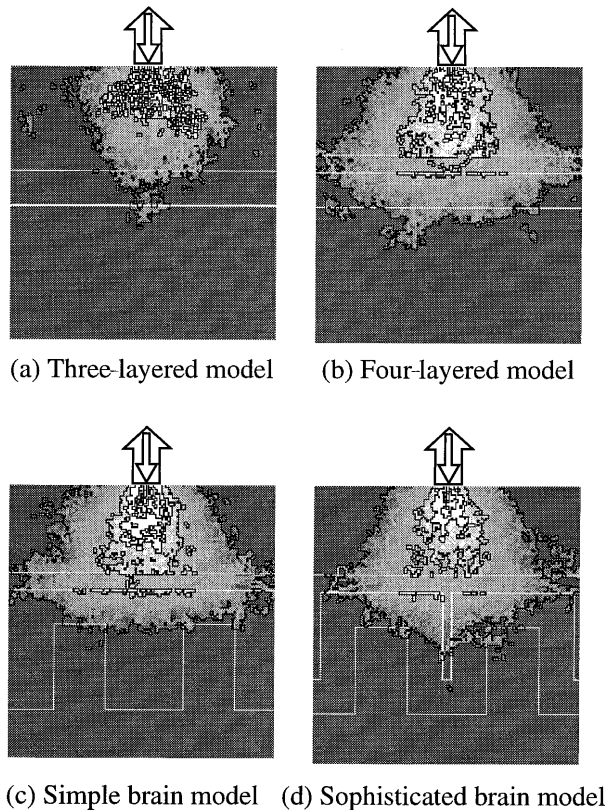


Fig. 9. Spatial sensitivity profiles with a detection fiber 30 mm distant from the light source along the vertical (y) axis.

a clear CSF layer increase slowly beyond a detection position of 25 mm whereas those of the three-layered model continue to increase steeply. It is obvious that the clear CSF layer considerably affects the mean optical path length at these large spacing. The features of light propagation in the adult head can thus be placed in these categories according to the detection position: (1) at small detection positions (≤ 15 mm) the mean optical path length is equivalent to the partial mean optical path length of the surface layer, i.e., the spatial sensitivity profile is confined to the surface layer; (2) at intermediate detection positions (≥ 15 mm, ≤ 25 mm) the partial mean optical path lengths of both the clear CSF and the gray-matter layer increase with the detection position, and the spatial sensitivity profile spreads laterally over the inner face of the surface layer and the gray-matter layer; and (3) at large detection positions (≥ 25 mm) the partial mean optical path lengths of the surface and the gray-matter layer remain approximately constant while that of the clear CSF layer increases with the detection position. The spatial sensitivity profile is distributed mainly around the surfaces that face the clear CSF layer except for the sites directly underneath the source and the detector. It is apparent that once light reaches the clear CSF, this layer starts to act as a conduit for the light that reaches the distant detector. Because little absorption occurs in the clear CSF layer, the intensity of detected light at large detection positions in the mod-

els with a clear CSF layer is much higher than that in the three-layered model without the clear CSF layer. The light that passes through the CSF layer only grazes the surface and the gray-matter layers, which therefore make little contribution to the optical path length. Thus the partial mean optical path lengths in the surface and the gray-matter layers increase only slowly with detection position. It is also notable that the presence of the clear CSF layer significantly reduces the light penetration into the deeper white-matter layer. As shown in Fig. 4, the partial mean optical path length of the white-matter layer in the models with a clear CSF layer are almost negligible whereas that in the three-layered model without the clear CSF layer steeply increases beyond a detection spacing of 40 mm. It should be emphasized here that the presence of the clear layer does not prevent light penetration into white matter. Indeed, the intensity of the detected light that has penetrated into the white matter is probably similar to that in the three-layered model; however, the increased intensity of the light guided to the detector through the CSF layer becomes the dominant component of the signal. Because in the clear-layer models, light penetration into the gray matter is predominantly confined to a shallow depth, the geometry of both the sulci and the boundary between the gray and the white-matter layers only slightly affect the partial mean optical path lengths and spatial sensitivity profiles. In the case in which both the source and the detector are placed along the axis of a slot, the light does penetrate deeper, but even then, it is still confined to the area around the sulcus and the light does not penetrate the white matter.

From the FEM predictions of the partial optical path lengths in the sophisticated brain model shown in Fig. 4(d), light detected at a spacing of 50 mm spends approximately 65% of its path length in the scalp and skull, 35% in the CSF, and 5% in the gray matter, with very little white-matter component. However, these ratios do not necessarily represent the contribution of each layer to the change in the output signal. The change in the output signal depends not only on the partial mean optical path length but also on the change in the absorption coefficient. Any layer in which no absorption change occurs does not contribute to the output signal, no matter how long the light path length in it. Similarly, the deeper area in which the partial mean optical path length is much shorter than in the shallow area can contribute significantly to the output signal if the absorption change there is much greater than that in the shallow area. This may explain why absorption changes caused by intracranial hemorrhage can be detected with NIRS instruments even if they occur in the white matter or in deeper areas of the gray matter.³⁸ This sort of drastic absorption change will also considerably affect the light propagation in the head and hence alter both the partial mean optical path lengths and the spatial sensitivity profile. For example, it is easy to imagine that if the CSF is replaced by blood in an epidural hemorrhage,

the CSF layer no longer works as a light guide. Accordingly the prediction of partial mean optical path length and spatial sensitivity profile for the models in this study cannot be used to analyze the signal contribution and interrogated area in cases in which drastic absorption changes occur in the head.

However, in most clinical NIRS studies, smaller absorption changes, for example, those that are due to mild hypoxia or changes in oxygenation state with brain activity and so on, are normally monitored. This sort of small absorption change should minimally affect the light propagation in the head, and hence the detected light distribution can be described by the spatial sensitivity profiles shown in Figs. 6–9. Because the change in the absorption coefficient depends on the blood content and there is virtually no absorption change in the CSF layer under normal conditions, the contribution of the CSF layer to the output signal is negligible. In this study the scalp (typically 5 mm thick) and the skull (typically 5 mm thick) were combined into one surface layer, and the partial optical path length of this combined layer is much greater than that of all other layers. The blood volume and hence the absorption coefficient of the scalp is much higher than those of the skull; however, in NIRS studies, the blood directly under the NIRS optodes may often be squeezed out because of optode pressure, thus reducing its contribution to the total absorption change signal. The light in the surface layer then passes through the skull, which, because of its low blood volume, also contributes little to any absorption change signal. This supposition is further borne out by the spatial sensitivity profile, which shows that this element of the signal arises mainly from the inner skull table. In the brain the blood volume in gray matter is approximately twice as much as that in white matter,³⁹ and hence the absorption change caused by oxygenation variation in gray matter is generally greater than that in white matter. Consequently, the actual contribution of the absorption change in the gray matter to the change in the detected NIRS signal is probably significantly greater under normal conditions and it probably reaches at least 20–30%. The success of experimental studies of cerebral-evoked response in adult humans provides further evidence for this conclusion.^{6,40–42}

6. Conclusions

In this study the effect on NIR signals of the layered surface tissues surrounding the brain in the adult head have been investigated by both time-of-flight measurements and mathematical predictions. The clear CSF layer significantly affects light propagation in the adult head once the spacing between source and detector is greater than 15 mm. At large source–detector spacing the detected light passes mainly through the CSF layer and this forces the sensitive region to be confined to a shallow section of the gray matter. The partial mean optical path lengths of both the surface and the gray-matter layers change only slowly once the detection position

exceeds 30 mm. This indicates that the contribution of changes in absorption in the gray matter to the NIRS signal is almost constant at these detection positions and its contribution probably reaches 20%–30%. Under these circumstances, it is difficult for NIRS to detect small oxygenation changes in the deeper areas of the gray and the white matter. The geometries of the sulci and the boundary between the gray- and the white-matter layers scarcely affect the optical path in the adult head.

This work was supported by the Japan Society for the Promotion of Science, Postdoctoral Fellowship for Research Abroad to E. Okada from April 1995 to March 1996, funding from the Engineering and Physical Research Council (UK) (GR/K07386, GR/G05100), the Wellcome Trust, and Hamamatsu Photonics KK. Some parts of these data were presented at a Society of Photo-Optical Instrumentation Engineers' Conference, "Photon Propagation in Tissues: Quantitation and Clinical Studies using Continuous Wave, Time, and Frequency Domain Technology" in Barcelona, Spain, in 1995.

References

1. F. F. Jöbsis, "Non invasive, infrared monitoring of cerebral and myocardial oxygen sufficiency and circulatory parameters," *Science* **198**, 1264–1267 (1977).
2. C. J. Aldrich, J. S. Wyatt, J. A. Spencer, E. O. R. Reynolds, and D. T. Delpy, "The effect of maternal oxygen administration of human fetal cerebral oxygenation measured during labour by near infrared spectroscopy," *Br. J. Obstet. Gynaecol.* **101**, 509–513 (1994).
3. J. S. Wyatt, D. T. Delpy, M. Cope, S. Wray, and E. O. R. Reynolds, "Quantification of cerebral oxygenation and haemodynamics in sick newborn infants by near infrared spectroscopy," *Lancet* **8515**, 1063–1066 (1986).
4. M. Ferrari, E. Zanette, I. Giannini, G. Sideri, C. Fieschi, and A. Carpi, "Effect of carotid artery compression test on regional cerebral blood volume, haemoglobin oxygen saturation and cytochrome-c-oxidase redox level in cerebrovascular patients," *Adv. Exp. Med. Biol.* **200**, 213–222 (1986).
5. N. B. Hampson, E. M. Camporesi, B. W. Stolp, R. E. Moon, J. E. Shook, J. A. Griebel, and C. A. Piantadosi, "Cerebral oxygen availability by NIR spectroscopy during transient hypoxia in humans," *J. Appl. Physiol.* **69**, 907–913 (1990).
6. Y. Hoshi and M. Tamura, "Detection of dynamic changes in cerebral oxygenation coupled to neuronal function during mental work in man," *Neurosci. Lett.* **150**, 5–8 (1993).
7. Y. A. B. D. Wickramasinghe, J. A. Crowe, and P. Rolfe, "Laser source and detector with single processor for a near infra-red medical application," in *IERE Progress Reports on Electronics in Medicine and Biology*, K. Copeland, ed. (Institution of Electronic and Radio Engineers, London, 1986), pp. 209–215.
8. M. Cope and D. T. Delpy, "System for long term measurement of cerebral blood and tissue oxygenation on newborn infants by near infrared transillumination," *Med. Biol. Eng. Comput.* **26**, 289–294 (1988).
9. B. Chance, M. Maris, J. Sorge, and M. Z. Zhang, "A phase modulation system for dual wavelength difference spectroscopy of haemoglobin deoxygenation in tissue," in *Time-Resolved Laser Spectroscopy in Biochemistry II*, J. R. Lakowicz, ed., *Proc. SPIE* **1204**, 481–491 (1990).
10. M. Miwa, Y. Ueda, and B. Chance, "Development of time resolved spectroscopy system for quantitative noninvasive tissue measurement," in *Optical Tomography, Photon Migration,*

- and Spectroscopy of Tissue and Model Media: Theory, Human Studies, and Instrumentation*, B. Chance and R. R. Alfano, eds., Proc. SPIE **2389**, 142–149 (1995).
11. D. T. Delpy, M. Cope, P. van der Zee, S. R. Arridge, S. Wray, and J. S. Wyatt, "Estimation of optical pathlength through tissue from direct time of flight measurement," *Phys. Med. Biol.* **33**, 1433–1442 (1988).
 12. P. van der Zee, M. Cope, S. R. Arridge, M. Essenpreis, L. A. Potter, A. D. Edwards, J. S. Wyatt, D. C. McCormick, S. C. Roth, E. O. R. Reynolds, and D. T. Delpy, "Experimentally measured optical pathlengths for the adult head, calf and forearm and the head of the newborn infant as a function of inter optode spacing," *Adv. Exp. Med. Biol.* **316**, 143–153 (1992).
 13. J. S. Wyatt, M. Cope, D. T. Delpy, P. van der Zee, S. R. Arridge, A. D. Edwards, and E. O. R. Reynolds, "Measurement of optical pathlength for cerebral near infrared spectroscopy in newborn infants," *Dev. Neurosci.* **12**, 140–144 (1990).
 14. A. Duncan, J. H. Meek, M. Clemence, C. E. Elwell, L. Tyszczyk, M. Cope, and D. T. Delpy, "Optical pathlength measurements on adult head, calf and forearm and the head of the newborn infant using phase resolved optical spectroscopy," *Phys. Med. Biol.* **40**, 295–304 (1995).
 15. A. Duncan, J. H. Meek, M. Clemence, C. E. Elwell, P. Fallon, L. Tyszczyk, M. Cope, and D. T. Delpy, "Measurement of cranial optical pathlength as a function of age using phase resolved optical spectroscopy," *Pediatr. Res.* **39**, 1–7 (1996).
 16. R. Nossal, J. Kiefer, G. H. Weiss, R. Bonner, H. Taitelbaum, and S. Havlin, "Photon migration in layered media," *Appl. Opt.* **27**, 3382–3391 (1988).
 17. H. Taitelbaum, S. Havlin, and G. H. Weiss, "Approximate theory of photon migration in a two-layer medium," *Appl. Opt.* **28**, 2245–2249 (1989).
 18. W. Cui and L. E. Ostrander, "The relationship of surface reflectance measurements to optical properties of layered biological media," *IEEE Trans. Biomed. Eng.* **39**, 194–201 (1992).
 19. M. Hiraoka, M. Firbank, M. Essenpreis, M. Cope, S. R. Arridge, P. van der Zee, and D. T. Delpy, "A Monte Carlo investigation of optical pathlength in inhomogeneous tissue and its application to near-infrared spectroscopy," *Phys. Med. Biol.* **38**, 1859–1876 (1993).
 20. E. Okada, M. Firbank, M. Schweiger, S. R. Arridge, J. C. Hebden, M. Hiraoka, and D. T. Delpy, "Experimental measurements on phantoms and Monte Carlo simulation to evaluate the effect of inhomogeneity on optical pathlength," in *Optical Tomography, Photon Migration, and Spectroscopy of Tissue and Model Media: Theory, Human Studies, and Instrumentation*, B. Chance and R. R. Alfano, eds., Proc. SPIE **2389**, 174–181 (1995).
 21. M. Firbank, M. Schweiger, and D. T. Delpy, "Investigation of 'light piping' through clear regions of scatter objects," in *Optical Tomography, Photon Migration, and Spectroscopy of Tissue and Model Media: Theory, Human Studies, and Instrumentation*, B. Chance and R. R. Alfano, eds., Proc. SPIE **2389**, 167–173 (1995).
 22. E. Okada, M. Firbank, and D. T. Delpy, "The effect of overlying tissue on the spatial sensitivity profile of near-infrared spectroscopy," *Phys. Med. Biol.* **40**, 2093–2108 (1995).
 23. A. H. Hielscher, H. Liu, B. Chance, F. K. Tittel, and S. L. Jacques, "Phase resolved reflectance spectroscopy on layered turbid media," in *Optical Tomography, Photon Migration, and Spectroscopy of Tissue and Model Media: Theory, Human Studies, and Instrumentation*, B. Chance and R. R. Alfano, eds., Proc. SPIE **2389**, 248–256 (1995).
 24. M. Firbank, S. R. Arridge, M. Schweiger, and D. T. Delpy, "An investigation of light transport through scattering bodies with non-scattering region," *Phys. Med. Biol.* **41**, 767–783 (1996).
 25. J. C. Schotland, J. C. Haselgrove, and J. S. Leigh, "Photon hitting density," *Appl. Opt.* **32**, 448–453 (1993).
 26. S. R. Arridge, "Photon-measurement density functions. Part I: analytical forms," *Appl. Opt.* **34**, 7395–7409 (1995).
 27. W. F. Cheong, S. A. Prahl, and A. J. Welch, "A review of the optical properties of biological tissues," *IEEE J. Quantum Electron.* **26**, 2166–2185 (1990).
 28. P. van der Zee, M. Essenpreis, and D. T. Delpy, "Optical properties of brain tissue," in *Photon Migration and Imaging in Random Media and Tissues*, R. R. Alfano and B. Chance, eds., Proc. SPIE **1888**, 454–465 (1993).
 29. M. Firbank, M. Hiraoka, M. Essenpreis, and D. T. Delpy, "Measurement of the optical properties of the skull in the wavelength range 650–950 nm," *Phys. Med. Biol.* **38**, 503–510 (1993).
 30. M. Firbank and D. T. Delpy, "A design for a stable and reproducible phantom for use in near infra-red imaging and spectroscopy," *Phys. Med. Biol.* **38**, 847–853 (1993).
 31. B. C. Wilson and G. Adam, "A Monte Carlo model for the absorption and flux distributions of light in tissue," *Med. Phys.* **10**, 824–830 (1983).
 32. P. van der Zee and D. T. Delpy, "Simulation of the point spread function for light in tissue by a Monte Carlo technique," *Adv. Exp. Med. Biol.* **215**, 179–191 (1987).
 33. M. S. Patterson, B. C. Wilson, and D. Wyman, "The propagation of optical radiation in tissue. I. Models of radiation transport and their application," *Lasers Med. Sci.* **6**, 155–168 (1990).
 34. J. J. Duderstadt and L. J. Hamilton, *Nuclear Reactor Analysis* (Wiley, New York, 1978), 140–144.
 35. A. Ishimaru, *Wave Propagation and Scattering in Random Media* (Academic, New York, 1978), Vol. 1.
 36. S. R. Arridge, M. Schweiger, M. Hiraoka, and D. T. Delpy, "A finite element approach for modeling photon transport in tissue," *Med. Phys.* **20**, 299–309 (1993).
 37. M. Schweiger, S. R. Arridge, M. Hiraoka, and D. T. Delpy, "The finite element method for the propagation of light in scattering media: boundary and source conditions," *Med. Phys.* **22**, 1779–1792 (1995).
 38. S. P. Gopinath, C. S. Robertson, R. G. Grossman, and B. Chance, "Near infrared spectroscopic localisation of intracranial hematomas," *J. Neurosurg.* **79**, 43–47 (1993).
 39. K. L. Leenders, D. Perani, A. A. Lammertsma, J. D. Heather, P. Buckingham, M. J. R. Healy, J. M. Gibbs, R. J. S. Wise, J. Hatazawa, S. Herold, R. P. Beaney, D. J. Brooks, T. Spinks, C. Rhodes, R. S. J. Frackowiak, and T. Jones, "Cerebral blood flow, blood volume and oxygen utilization," *Brain* **113**, 27–47 (1990).
 40. A. Villringer, J. Planck, C. Hock, L. Schleinkofer, and U. Dirnagl, "Near infrared spectroscopy (NIRS): a new tool to study hemodynamic changes during activation of brain function in human adults," *Neurosci. Lett.* **154**, 401–404 (1993).
 41. G. Gratton, P. M. Corballis, E. Cho, M. Fabiani, and D. C. Hood, "Shades of gray matter: noninvasive optical images of human brain responses during visual stimulation," *Psychophysiology* **32**, 505–509 (1995).
 42. J. H. Meek, C. E. Elwell, M. J. Khan, J. Romaya, J. S. Wyatt, D. T. Delpy, and S. Zeki, "Regional changes in cerebral haemodynamics as a result of a visual stimulus measured by near infrared spectroscopy," *Proc. R. Soc. London Ser. B* **261**, 351–356 (1995).